ELSEVIER

Polymer 40 (1999) 2837–2844

polymer

Liquid–liquid phase separation and its effect on crystallization in the extruded polypropylene/ethylene–propylene–rubber blend

Sung Wook Lim[a], Kwang Hee Lee[a,*], Chang Hyung Lee[b]

[a]*School of Chemical Science and Engineering, Inha University, Inchon 402-751, South Korea*
[b]*Materials Analysis Division, Department of Chemistry, National Institute of Technology and Quality, 2, Jungang-dong, Kwacheon city, Kyunggi-do 427-010, South Korea*

Received 8 April 1998; revised 5 June 1998; accepted 18 June 1998

Abstract

The liquid–liquid (L–L) phase separation and its effect on crystallization in polypropylene (PP)/ethylene–propylene–rubber (EPR) blend obtained by melt extrusion were investigated by time-resolved light scattering (TR-LS), optical microscope and small-angle X-ray scattering (SAXS). The existence of the lower critical solution temperature (LCST) was found by the kinetic analysis of the L–L phase separation, that is, the apparent diffusion coefficient of spinodal decomposition (SD), obtained by the TR-LS, decreased with increasing temperature. The L–L phase-separated specimen at 190°C for various time periods was subjected to a temperature-drop to 130°C for the isothermal crystallization and then investigated effect of L–L phase separation on crystallization. Memory of L–L phase separation via SD remained even after crystallization and crystallization proceeded only in PP-rich phases. The crystallization rate decreased with increasing L–L phase-separated time at 190°C. The rapid crystallization for short L–L phase-separated time could be ascribed to the elevation of chain mobility of PP by relatively higher amounts of EPR in PP-rich phases. The amount of EPR between PP lamellae in PP-rich phases was quantified using the correlation function, which is given by the fourier transform of the SAXS intensity.

Keywords: Polypropylene; Ethylene–propylene–rubber; Phase separation

1. Introduction

Polypropylene/ethylene–propylene–rubber (PP/EPR) blend is an injection-molded thermoplastic applied widely for automotive parts. In order to improve the recyclability and lighten the car body, recently work has progressed on developing a new level of PP/EPR blend with the outstanding physical property balance.

In a PP/EPR blend obtained by melt extrusion, we found that liquid–liquid (L–L) phase separation at high temperatures is very similar to the spinodal decomposition (SD) indicative of the partially misicible system, i.e. low critical solution temperature (LCST)/upper critical solution temperature (UCST). This may be that the conventional interpretation and understanding for the morphological formation in a PP/EPR blend is completely changed. It was known that a PP/EPR blend is highly immiscible at all temperatures [1] and, therefore, so far the morphology of a PP/EPR blend was interpreted on the basis of the immiscible system. This is motivated to inquire L–L phase separation in a PP/EPR blend which was believed to be a totally immiscible system.

Many experimental studies on PP/EPR blend was devoted to the morphology of EPR, i.e. the shape and size distribution of the EPR domains, adhesion at the interface, nature and structure of the EPR domains [2–5]. However, it is widely accepted that properties of the blend in crystalline polymer/noncrystalline polymer blends depend on their crystalline structure, crystalline structure of PP matrix in a PP/EPR blend may also affect the mechanical properties. Recently, Nomura et al. [6] reported a new structural model which improves the stiffness and surface hardness by controlling PP crystalline lamellar structures of a PP/EPR blend. Coppola et al. [7] found a very close correlation between crystallization conditions and mechanical property in a PP/EPR blend. The formation of the crystalline structure relates to L–L phase separation when the blend has an immiscibility gap, i.e. UCST/LCST. In the blend system with LCST, L–L phase separation would be able to precede crystallization and have a significant influence

* Corresponding author. E-mail: khlee@munhak.inha.ac.kr

0032-3861/99/$ - see front matter
PII: S0032-3861(98)00493-5

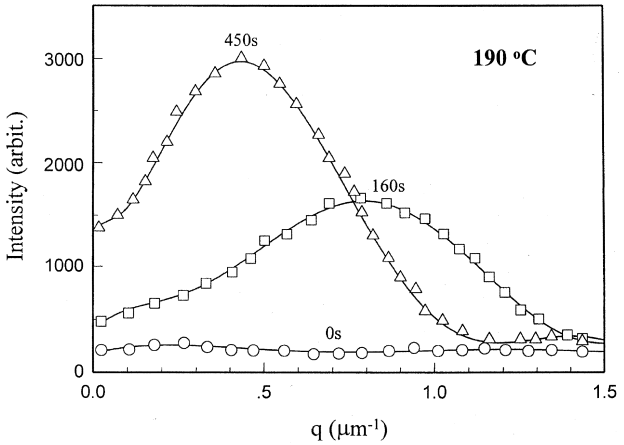

Fig. 1. Change in light scattering profiles of a 50/50 PP/EPR blend during L–L phase separation at 190°C.

on crystallization. Therefore, we need to know information on both phase behavior and its effect on crystallization which will result in control of physical properties of the materials.

In this paper, we first carried out time-resolved light scattering (TR-LS) studies of the kinetics of the L–L phase separation to determine the phase behavior and then TR-LS, SAXS and optical microscope (OM) studies to investigate the effect of L–L phase separation on crystallization.

2. Experimental

2.1. Materials

The isotactic PP was supplied by LG Chemical, Ltd. The specific gravity and melt flow rate (MFR) are 0.91 and 30,

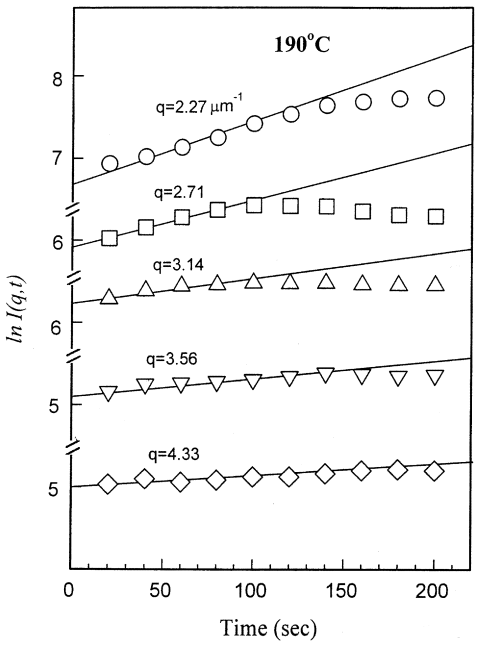

Fig. 2. Change of the scattered light intensity at various **q** with time for a 50/50 PP/EPR blend at 190°C.

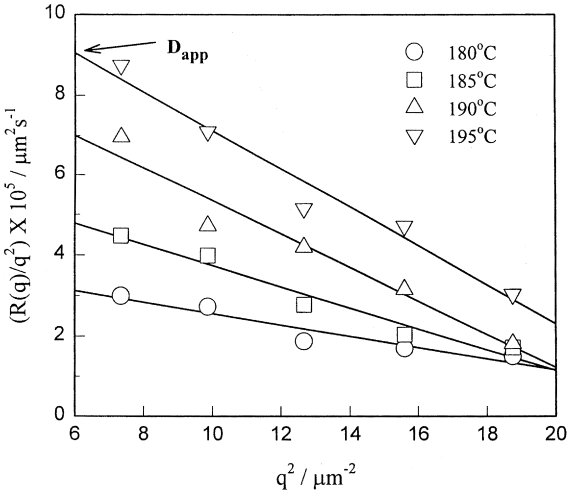

Fig. 3. R(**q**)$\mathbf{q}^2$ versus $\mathbf{q}^2$ plot in a 50/50 PP/EPR blend.

respectively. The EPR used in this work contains 67 mol% ethylene and the Mooney viscosity, ML_{1+4} (125°C) is 12. The 50/50 (by weight) blend was prepared by extruding the two components with a twin-screw extruder at about 220°C. After extrusion, the blend was cooled to room temperature and granulated to pellets.

2.2. TR-LS and OM

A thin-layer specimen (ca. 15 μm thick) was prepared by pressing the blend pellets between two cover glasses at 190°C. Immediately after the melt-pressing, the specimen was quickly transferred into a hot stage on light scattering photometer equipped with a CCD (charge-coupled device) camera [8] and the kinetics of the L–L phase separation was investigated.

The L–L phase-separated specimen at 190°C for t_S was rapidly transferred into a light scattering hot stage set at 130°C for the isothermal crystallization and then the effect of L–L phase separation on crystallization was investigated. The time t_S is the time spent for L–L phase separation at 190°C. A polarized He–Ne gas laser of 632.8 nm wavelength was applied to the film specimen. We employed the V_v geometry in which the optical axis of the analyzer was set parallel to that of the polarizer.

The final morphology of the crystallized specimen at 130°C after t_S was also observed under an optical microscope (OM).

2.3. SAXS

The pellets were annealed, i.e. phase-separated between metal plates at 190°C for t_S = 1, 5 and 10 min. The L–L phase-separated specimen was rapidly transferred into another hot chamber set at 130°C and was crystallized. Then the specimen was cooled to room temperature and cut into thin stripes (7 mm × 5 mm × 1 mm). This crystallized specimen was used for SAXS.

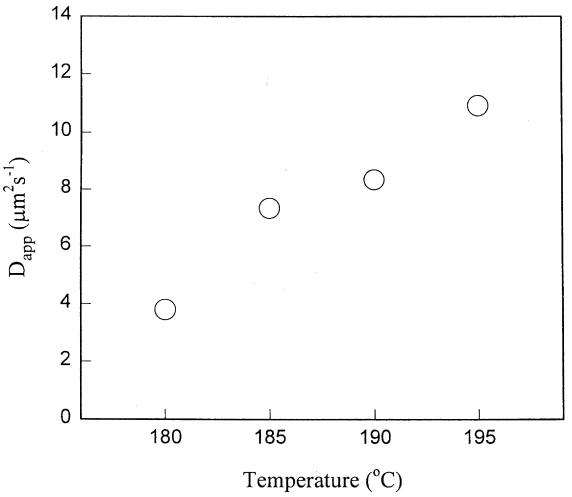

Fig. 4. Temperature dependence of apparent diffusion coefficient D_{app} in a 50/50 PP/EPR blend.

The X-ray beam was from synchrotron radiation, beam line 3C2 at Pohang Accelerator Laboratory, Pohang, South Korea. The storage ring was operated at an energy level of 2 GeV. The SAXS employs a point focusing optics with a Si double crystal monochromator followed by a bent cylindrical mirror. The incident beam intensity of 0.149 nm wavelength was monitored by an ionization chamber for the correction of a minor decrease of the primary beam intensity during the measurement.

The scattering intensity, I, was corrected for background scattering. Then, the scattering intensity by thermal fluctuations was subtracted from the SAXS profile $I(\mathbf{q})$ by evaluating the slope of a $I(\mathbf{q})\mathbf{q}^4$ vs $\mathbf{q}^4$ plots [9] at wide scattering vectors $\mathbf{q}$, where $\mathbf{q}$ is $(4\pi/\lambda)\sin\theta$, λ and θ being the wavelength and scattering angle, respectively. The correction for smearing effect by the finite cross section of the incident beam was not necessary for the optics of SAXS with point focusing.

3. Results and discussion

3.1. LCST behavior

The extruded specimens were held at various temperatures and then the L–L phase separation behavior was investigated. Fig. 1 shows the change of the scattering profiles with L–L phase separation time at 190°C. Note that, at $t = 0$, the scattering intensity is very weak and it has no $\mathbf{q}$ dependence, suggesting that the blend just after the re-melting at 190°C is a nearly homogeneous blend. It implies that the phase dissolution had took place before the measurement at 190°C. The homogeneous blend starts to phase-separate by annealing at 190°C, as shown by the increase in the scattering intensity. The appearance of a scattering peak suggests that the separation occurs via the spinodal decomposition mechanism. To confirm this point, we analyzed the early stage on the basis of the linearized Cahn–Hilliard theory [10,11].

In the early stage of spinodal decomposition, the scattered intensity I is expected to increase exponentially with time [11];

$$I(\mathbf{q}, t) = I(\mathbf{q}, 0)\exp[2R(\mathbf{q})t] \quad (1)$$

The amplification factor $R(\mathbf{q})$ is given by

$$R(\mathbf{q}) = -M\mathbf{q}^2(\partial^2 f/\partial c^2 + 2\kappa\mathbf{q}^2) \quad (2)$$

where f is the local free energy of mixing, c is the concentration, κ is the concentration-gradient energy coefficient and M is the mobility. According to Eq. (1), a plot of ln I vs time t at a fixed $\mathbf{q}$ should yield a straight line of slope $2R(\mathbf{q})$. The linear relationship is realized for the L–L phase separation in a 50/50 PP/EPR blend as shown in Fig. 2, indicating that the initial stage can be described by the linearized theory.

Fig. 3 shows $R(\mathbf{q})/\mathbf{q}^2$ vs $\mathbf{q}^2$. As expected from Eq. (2), the plot yields a straight line, indicating again that the initial stage can be described with the framework of the linearized theory. By the interception of $R(\mathbf{q})/\mathbf{q}^2$ at $\mathbf{q}^2 = 0$, one can obtain apparent mutual diffusion coefficient D_{app} given by [12]

$$D_{app} = -M(\partial^2 f/\partial c^2) \propto D_c[|\chi - \chi_S|/\chi_S] \propto T|T - T_S| \quad (3)$$

where D_c is the self-diffusion coefficient for translational diffusion, χ is the interaction parameter, χ_S is the χ at the spinodal temperature and T_S is the spinodal temperature.

The values of D_{app} were obtained at various temperatures. The results are shown in Fig. 4 as a function of temperature. D_{app} increases with temperature. The increase of D_{app} with increasing temperature is expected in the LCST system, since the quench depth $|T - T_S|$ increases with temperature (see Eq. (3)). The increase of D_{app} was observed in the LCST system [12].

A supplemental evidence of L–L phase separation induced by SD at 190°C was nicely given by observing a structure formation at 130°C. If one extrapolates the results in Fig. 4 to 130°C, the value of D_{app} at this temperature is expected to be very low. This implies that L–L phase separation rate may be negligible at 130°C. On the other hand, the crystallization rate of PP is very high so that crystallization is completed in about 4 s (which will be discussed in Fig. 8). In such a case, it is well known that the L–L phase-separated morphology, i.e. the periodic and interconnected structure, is preserved during the crystallization process [13]. Fig. 5 shows a typical SEM micrograph of a blend crystallized at 130°C after $t_S = 5$ min. The SEM observation was carried out after solvent etching with xylen so that the remaining material may be PP. As expected, a highly interconnected PP phase with unique periodicity is seen in the micrograph. Connectivity of phases is an important morphological feature of SD.

Further evidence for the SD process at 190°C is shown in Fig. 6. The phases are interconnected with each other

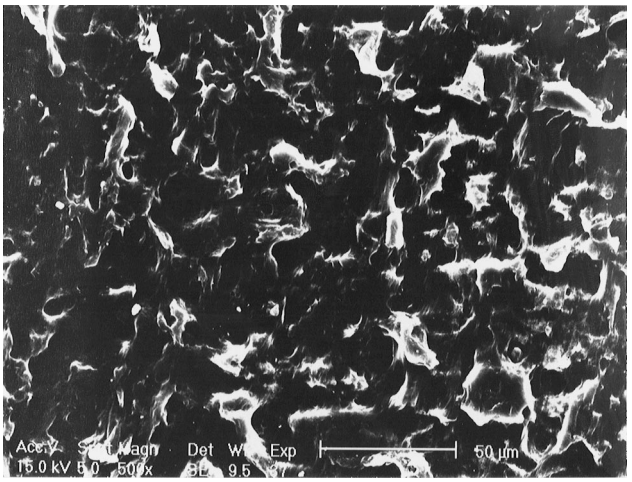

Fig. 5. Scanning electron micrograph of a 50/50 PP/EPR blend after t_S = 5 min.

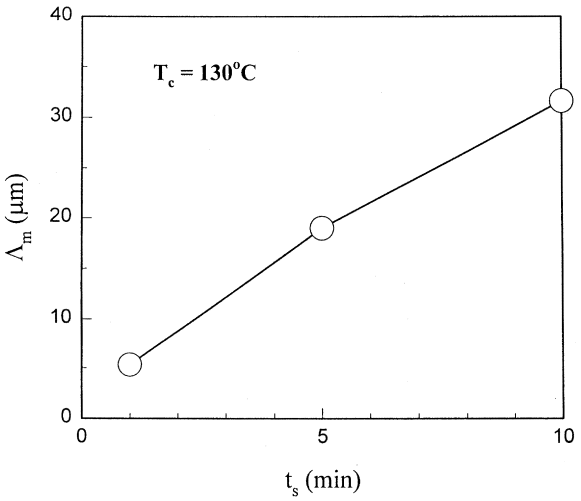

Fig. 7. Change of Λ_m with t_S.

[Fig. 6(a)]. The white stripes seemed to be crystalline fibril as seen in dark parts and, hence, the dark parts may be the PP-rich phases. At the later stage of L–L phase separation, the phase connectivity seems to grow in size while maintaining their connectivity [Fig. 6(b)] and eventually breaks up into macrospheres [Fig. 6(c)]. These characteristics agree with Cahn's prediction of SD mechanism. The increase of the interconnected/periodic length (Λ_m) with t_s is clearly seen also in Fig. 7. The values of Λ_m were obtained by applying the Bragg equation to the peak position of the light scattering profiles.

Based on the previous results, a scenario of the melt extrusion to yield near the homogeneous blend may be given as follows: under the high shear rate in the extruder, phase diagram elevated over the barrel temperature and one phase region becomes wide. Thus, the blend could be done in a wide temperature window for dissolution to get a homogeneous mixture. However, once the melt is extruded out from the nozzle, the shear rate turns out to be zero and LCST will immediately go down to the state without shear so that the SD will proceed until the system is cooled down to crystallization. The fast crystallization prevents further L–L phase separation. Finally the melt extruded sample shows state close to homogeneity.

3.2. Effect of L–L phase separation on crystallization

The specimens proceeded by L–L phase-separation at 190°C for t_S were then allowed to crystallize by rapid

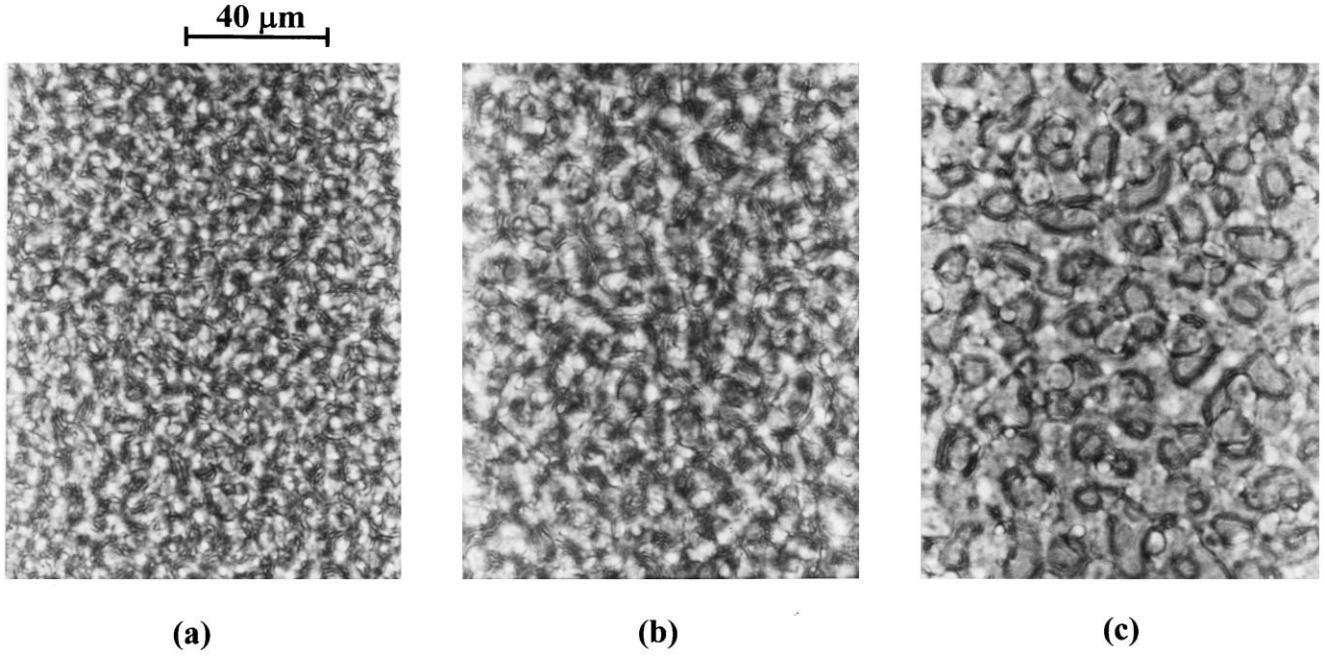

Fig. 6. Optical micrographs of a 50/50 PP/EPR blend crystallized at 130°C after: (a) t_S = 1 min; (b) t_S = 5 min; and (c) t_S = 10 min at 190°C.

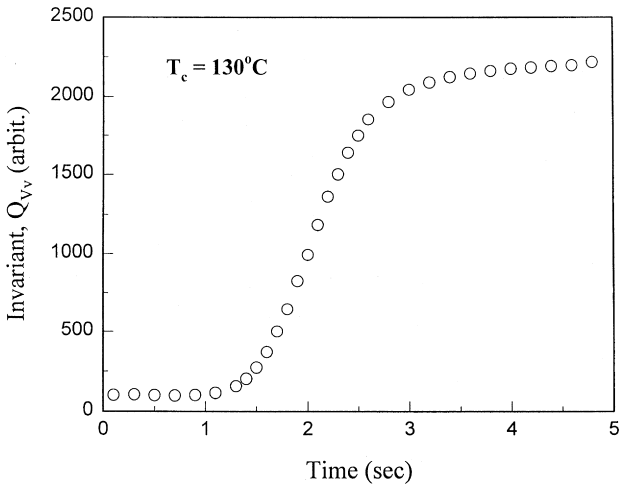

Fig. 8. Time variation of the invariant QV_v in a 50/50 PP/EPR blend during crystallization at 130°C after $t_S = 5$ min.

temperature drop to a light scattering hot stage set at 130°C for the isothermal crystallization.

To discuss the crystallization process, it is convenient to employ the integrated intensity, invariant Q, defined by [14]

$$Q = \int_0^\infty I(\mathbf{q})\mathbf{q}^2 \mathrm{d}\mathbf{q} \tag{4}$$

The time variation of the invariant in the V_v mode (parallel polarization), QV_v, is shown in Fig. 8. QV_v keeps constant in a limited value, increases rapidly and then levels off. A finite value at time zero may be ascribed to the density fluctuation formed by SD at 190°C before crystallization onset. At the early stage, the constant value with time implies that L–L phase separation no longer proceeds. Further, recalling the result in Fig. 4 that the value of D_{app}, i.e. L–L phase separation rate at 130°C is expected to be negligible, the rapid increase after early stage should be ascribed to the PP crystallization. The morphology can be

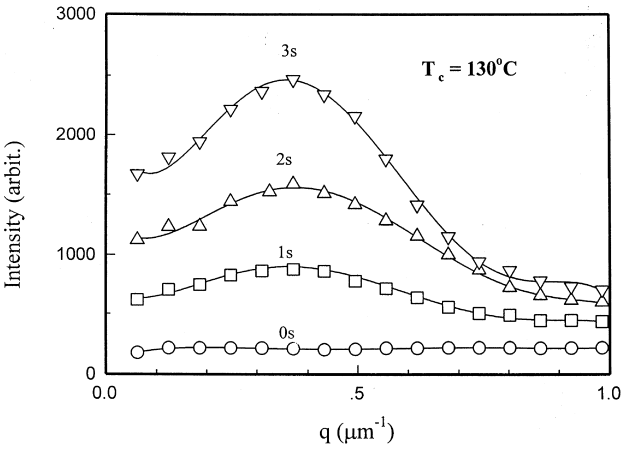

Fig. 9. Change in light scattering profiles of a 50/50 PP/EPR blend during crystallization at 130°C after $t_S = 5$ min.

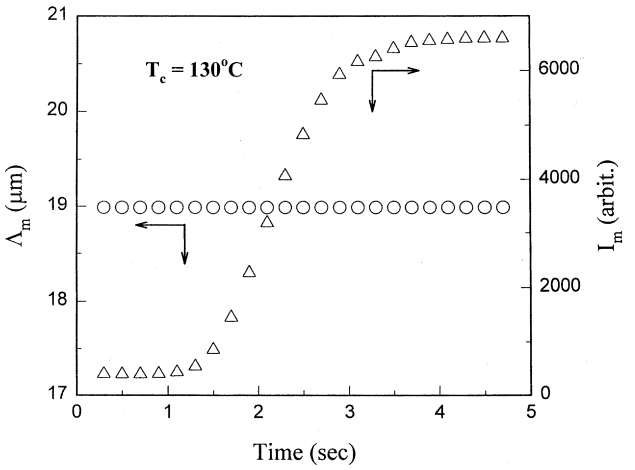

Fig. 10. Time variation of the periodic length Λ_m and the peak intensity I_m during crystallization at 130°C after $t_S = 5$ min.

understood in detail by investigating the V_v scattering profiles and their time variation.

Fig. 9 shows the change in the V_v scattering profiles during crystallization at 130°C. The peak position, indicative of Λ_m caused by SD at 190°C, keeps constant and its intensity (I_m) increases. The time variation of Λ_m and I_m is shown in Fig. 10. Λ_m is constant with time, supporting that L–L phase separation no longer proceeds during crystallization. On the other hand, I_m increases with time. Combining the result I_m with the Λ_m result, it can be concluded that crystallization takes place only in PP-rich phases and the increased density difference between EPR and PP-rich phases resulting from the crystallization contributes to an increase I_m without time variation of Λ_m. The crystallization only in PP-rich phases can be confirmed by OM. The white stripes seemed to be crystalline fibril as seen only in dark parts in Fig. 6.

To discuss the effect of the L–L phase separation structure on crystallization kinetics, one can use the TR-LS. Since the rapid increase in QV_v was ascribed to the crystallization (note the discussion in Fig. 8), QV_v can

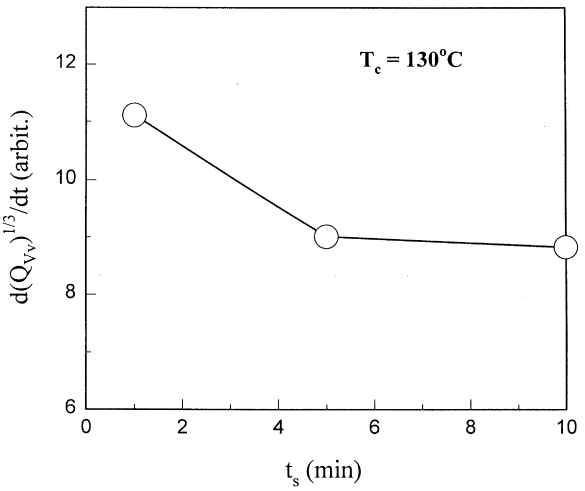

Fig. 11. Change of the G with t_S.

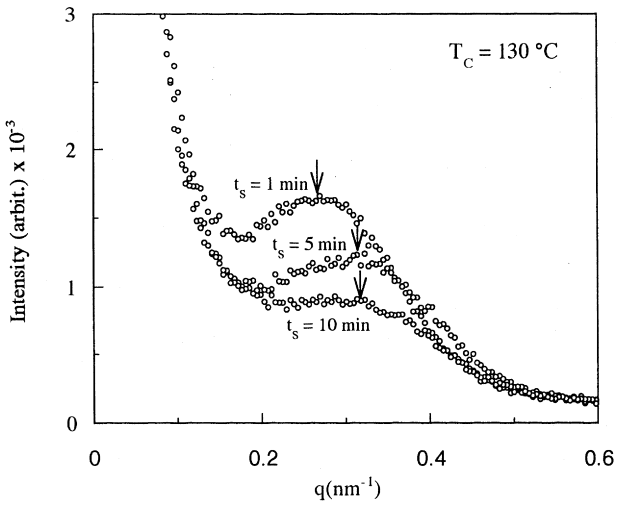

Fig. 12. SAXS profiles of a 50/50 PP/EPR blend crystallized at 130°C after $t_S = 1$, 5 and 10 min.

be described by [14]

$$QV_v \propto \phi_a(1-\phi_a)(\alpha_a - \alpha_0) \tag{5}$$

where ϕ_a is the volume fraction of crystalline aggregate, α_a and α_0 is the polarizability of crystalline aggregate and the melt, respectively. At the early stage of the crystallization, Eq. (5) is approximated by

$$QV_v \propto \phi_a(\alpha_a - \alpha_0) \tag{6}$$

At the early stage of crystallization, QV_v is assumed to be proportional to the volume fraction of crystallite so that the linear growth rate of crystallite G is given by

$$G \propto \mathrm{d}(QV_v)^{1/3}/\mathrm{d}t \tag{7}$$

Hence one can estimate G from the initial slope of the time variation of $(QV_v)^{1/3}$. The values of G estimated by Eq. (7) are shown as a function of t_S in Fig. 11. G decreases with t_S; G for $t_S = 5$ and 10 min is lower than that for $t_S = 1$ min. This may come from the difference in the amount of the EPR in PP-rich phases. The difference of the amount of EPR in PP-rich phases with t_S seems to originate from SD process at 190°C before crystallization. It is well known that SD renders the periodic concentration fluctuation. The growth of concentration fluctuation is realized by the up-hill diffusion; A molecules diffuse into A-rich regions from B-rich regions. So, in PP/EPR blend, EPR chains are forced to move from PP-rich regions to EPR-rich phases; as the L–L phase separation proceeds, the amount of EPR in PP-rich phases should be decreased by SD. In PP-rich phases, the T_g increases with decreasing the amount of EPR. Note that T_g in PP is higher than that in EPR. Higher T_g decreases diffusion coefficients so that the crystallization rate is reduced. Crystallization rates consist of nucleation rate and diffusion rate. The smaller amount of EPR in PP-rich phases by SD process may retard the crystallization rate and thereby the slow crystallization rate for $t_S = 5$ and 10 min can be interpreted.

To estimate the amount of the EPR in PP-rich phases, we studied SAXS. Since L–L phase separation in size is too high to be detected in SAXS, the information obtained from SAXS should correspond to the crystalline lamellar morphology.

Fig. 12 shows the SAXS profiles. From the peak position of the SAXS profiles, the long period L_B can be obtained by the Bragg equation. Other parameters related to lamellar morphology can be estimated from the correlation function $K_1(z)$, which is given by the Fourier transform of the scattering intensity $I(\mathbf{q})$ [15]:

$$K_1(z) = \int_0^\infty \mathbf{q}^2 I(\mathbf{q})\cos(\mathbf{q}z)\mathrm{d}\mathbf{q} \tag{8}$$

where z is the coordinate along which the electron density distribution is measured. The approach to estimate variables related to lamellar morphology is illustrated in Fig. 13(a), which shows a typical $K_1(z)$ obtained for $t_S = 5$ min. The results for $t_S = 1$ and 10 min are shown in Fig. 13(b). The position of the first maximum indicates the long spacing L_c^M, which means the most probable next-neighbor distance of the lamellae. Another important parameter is the crystalline lamellar thickness. The thickness may be calculated from the baseline procedure [15]. The extrapolation of the initial

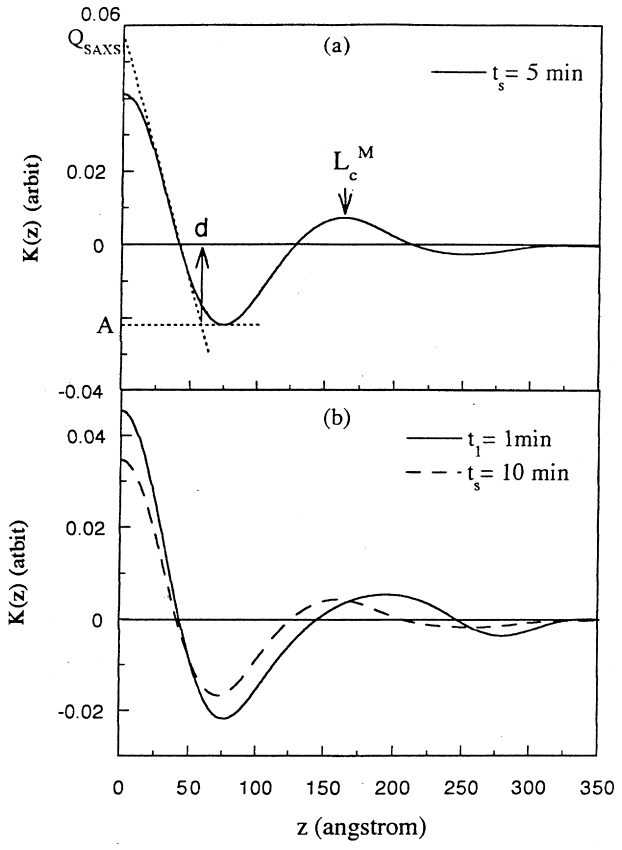

Fig. 13. Correlation function of a 50/50 PP/EPR blend crystallized at 130°C: (a) after $t_S = 5$ min; and (b) $t_S = 1$ and 10 min.

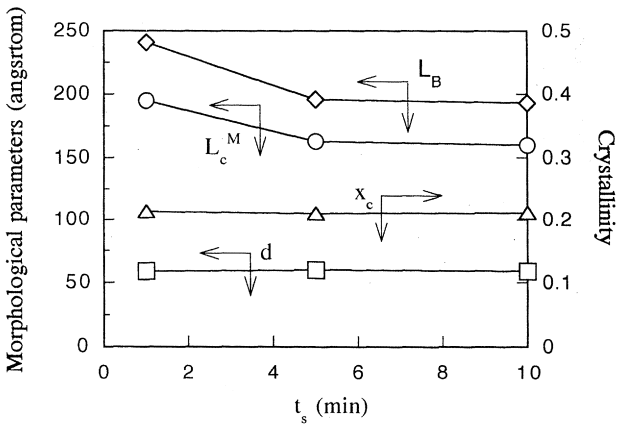

Fig. 14. Morphological parameters by SAXS and DSC as a function of t_S: L_B, the long period by the Bragg equation; L_c^M, the long period by the correlation function method; d, lamellar thickness by the correlation function method; X_c, the overall crystallinity by DSC.

slope for the $K_1(z)$ intersects the base line $K_1(z) = -A$ at $z = d$, the average thickness of the crystalline region. Here the base line is the horizontal line for the plateau region of the first minimum of $K_1(z)$ and the slope $dK_1(z)/dz$ is given by

$$dK_1(z)/dz = -(Q_{SAXS} + A)/d \quad (9)$$

where Q_{SAXS} is the invariant which is obtained by extrapolating $K_1(z)$ to $z = 0$. On the other hand, the heat of fusion ΔH_{pp} by using DSC was about 45 J g^{-1} for all specimens tested. Then the overall crystallinity X_c was evaluated by calculating $\Delta H_{pp}/\Delta H^{\circ}_{pp}$, where ΔH°_{pp} is the heat of fusion 100% crystalline PP (from literature data $\Delta H^{\circ}_{pp} = 209$ J g^{-1} [16]). The morphological parameters obtained by SAXS and DSC are shown as a function of t_S in Fig. 14.

For $t_S = 1$ min, the long period (L_B and L_c^M) is higher than that for $t_S = 5$ and 10 min. Taking account of constant lamellar thickness and crystallinity (independent of t_S), it may suggest that a large amount of EPR is entrapped between PP crystalline lamellae in PP-rich phases. The high concentration of EPR between lamellae can be caused by rejection of noncrystalline EPR components on the thickness scale of lamellae during crystallization. Such a rejection is often found in high crystallization rate [17–21]. The high crystallization rate is shown in Fig. 11, G for $t_S = 1$ min is higher than that for $t_S = 5$ and 10 min.

For $t_S = 5$ and 10 min, the long period is smaller than that for $t_S = 1$ min. This may be that a substantial amount of EPR should be trapped between crystalline fibrils consisting of lamellar bundles in PP-rich phases. The low concentration of EPR between lamellae can be assigned to the rejection of EPR on the thickness scale of fibril during crystallization. A interfibril rejection is found in low crystallization rates [17–21]. The crystallization rate for $t_S = 5$ and 10 min is relatively low as shown in Fig. 11.

Combining the G results discussed in Fig. 11 with the long period results, the dependence of G on t_S is explained by the change of the chain mobility of PP which results from the EPR concentration in PP-rich phases via SD, with increasing t_S, the amount of the EPR in PP-rich phases decreased and its decrease retarded the crystallization rate. Both the crystallization rate in Fig. 11 and the long period in Fig. 14 exhibit identical t_S dependence and thereby further support the previous interpretation.

4. Conclusions

Miscibility in the melt-extruded blend of PP/EPR was investigated by TR-LS and microscopy measurement. Then, LCST phase behavior was found to exist in the PP/EPR blend. For the melt-extruded blend near to homogeneity, one possible explanation could be that LCST might be elevated over the barrel temperature under the high shear rate in extruder, and therefore, blending could be done in one phase region.

The effect of L–L phase separation on the crystalline morphology produced by subsequent crystallization was discussed. The crystallization took place only in PP-rich phases so that the memory of SD (the periodic structure) was preserved. The crystallization rate decreased with the L–L phase separation time before crystallization. By a series of crystalline morphological parameters by SAXS and DSC analyses, it was shown that the amount of the EPR in PP-rich phases formed by SD deeply related to the crystallization rate and crystalline morphology, the amount of the EPR in PP rich phases decreased with increasing L–L phase separation time and its decrease induced the lower crystallization rate and the smaller long period.

Acknowledgements

This research was supported by the Korea Ministry of Education Research Fund for Advanced Materials in 1997 and LG Chemical Ltd.

References

[1] Moore EP Jr. Polypropylene handbook. Munich: Hanser, 1996:218.
[2] Jancar J, DiBenedetto AT. J Mater Sci 1995;30:1601.
[3] Yamaguchi M, Miyta H, Nitta KH. J Polym Sci, Polym Phys Edn 1997;35:953.
[4] Mirabella FM Jr. J Polym Sci, Polym Phys Edn 1994;32:1205.
[5] Yokoyama Y, Ricco T. J Appl Polym Sci 1997;66:1007.
[6] Nomura T, Nishino T, Iwanami K, Yokomizo K, Kitano K, Toki S. J Appl Polym Sci 1995;55:1307.
[7] Coppola F, Greco R, Martuscelli E. Polymer 1988;29:963.
[8] Lee CH, Saito H, Inoue T. Macromolecules 1995;28:8096.
[9] Koberstein JJ, Morra B, Stein RS. J Appl Crystallogr 1980;13:34.
[10] Chan JW, Hilliard JE. J Chem Phys 1958;28:258.
[11] Chan JW. J Chem Phys 1965;42:93.
[12] Hashimoto T, Kumaki J, Kawai H. Macromolecules 1983;16:641.
[13] Inaba N, Yamada T, Suzuki S, Hashimoto T. Macromolecules 1986;19:1690.

[14] Koberstein T, Russell TP, Stein RS. J Polym Sci Polym Phys Ed 1979;17:1719.
[15] Strobl GR, Schneider MJ, Voigt-Martin IG. J Polym Sci, Polym Phys Edn 1980;18:1361.
[16] Wunderlich B. Macromolecular physics. New York: Academic Press, 1973.
[17] Keith HD, Padden FJ Jr. J Appl Phys 1964;35:1270.
[18] Keith HD, Padden FJ Jr. J Appl Phys 1963;34:2409.
[19] Warner FP, Macknight WJ, Stein RS. J Polym Sci, Polym Phys Edn 1977;15:2113.
[20] Stein RS, Khambatta FB, Warner FP, Russell TP, Escala A, Balizer E. J Polym Sci, Polym Phys Edn 1978;16:313.
[21] Hudson SD, Davis DD, Lovinger AJ. Macromolecules 1992;25: 1759.